Optics & Laser Technology 161 (2023) 109161

Contents lists available at ScienceDirect

Optics and Laser Technology

journal homepage: www.elsevier.com/locate/optlastec

Full length article

Single-shot selective femtosecond and picosecond infrared laser crystallization of an amorphous Ge/Si multilayer stack

V.A. Volodin [a,b], Yuzhu Cheng [b], A.V. Bulgakov [c], Y. Levy [c], J. Beránek [c,d], S.S. Nagisetty [c,e], M. Zukerstein [c], A.A. Popov [f], N.M. Bulgakova [c,*]

[a] Rzhanov Institute of Semiconductor Physics SB RAS, 630090 Novosibirsk, Russia
[b] Novosibirsk State University, 630090 Novosibirsk, Russia
[c] HiLASE Centre, Institute of Physics of the Czech Academy of Sciences, 25241 Dolní Břežany, Czech Republic
[d] Czech Technical University, Faculty of Nuclear Sciences and Physical Engineering, Praha Czech Republic
[e] Coherent LaserSystems GmbH & Co. KG, Hans Boeckler Str. 12, 37079 Göttingen, Germany
[f] Valiev Institute of Physics and Technology, Yaroslavl Branch, Russian Academy of Sciences, 150007 Yaroslavl, Russia

ARTICLE INFO

Keywords:
Germanium/silicon multilayer stack
Ultrashort infrared laser crystallization
Selective crystallization
Explosive low-temperature crystallization
Raman spectroscopy
Nonlinear light absorption

ABSTRACT

Pulsed laser crystallization is an efficient annealing technique to obtain polycrystalline silicon or germanium films on non-refractory substrates. This is important for creating "flexible electronics" and can also be used to fabricate thin-film solar cells. In this work, near- and mid-infrared femtosecond and picosecond laser pulses were used to crystallize a Ge/Si multilayer stack consisting of alternating amorphous thin films of silicon and germanium. The use of infrared radiation at wavelengths of 1030 and 1500 nm with photon energies lower than the optical absorption edge in amorphous silicon allowed obtaining selective crystallization of germanium layers with a single laser shot. The phase composition of the irradiated stack was investigated by the Raman scattering technique. Several non-ablative regimes of ultrashort-pulse laser crystallization were found, from partial crystallization of germanium without intermixing the Ge/Si layers to complete intermixing of the layers with formation of Ge_xSi_{1-x} solid alloys. The roles of single- and two-photon absorption, thermal and non-thermal (ultrafast) melting processes, and laser-induced stresses in selective pico- and femtosecond laser annealing are discussed. It is concluded that, due to a mismatch of the thermal expansion coefficients between the adjacent stack layers, efficient explosive solid-phase crystallization of the Ge layers is possible at relatively low temperatures, well below the melting point.

1. Introduction

Low-temperature crystallization of thin amorphous semiconductor films is in high demand for creation of "flexible electronics" devices. Recently, germanium thin films with a record-high hole mobility were obtained on flexible plastic using post-growth annealing at relatively low temperature of 500 °C [1]. However, in order to use inexpensive plastics as flexible substrates, it is necessary to considerably reduce the temperature of the processes below 120 °C. This cannot be done for silicon and germanium films even using metal-induced crystallization [2]. Pulsed laser annealing appears to be the only suitable technique for low-temperature crystallization of amorphous semiconductor films on non-refractive substrates [3–12]] which can also be efficiently used for structuring of materials [13–16].

When thin layers of a narrow-band semiconductor (for example Ge) are surrounded by layers of amorphous silicon, the pulsed infrared laser annealing (PIRLA) technique allows to selectively crystallize regions that absorb infrared light, i.e., Ge layers in our case, if the laser photon energy is below the optical absorption edge of a-Si (1.3–1.4 eV [17,18]). Such multilayer (ML) stack structures can be used in *p-i-n* photodiodes or solar cells [19]. Recently, attempts were made to selectively crystallize germanium in amorphous Ge/Si MLs but, since a non-infrared ($\lambda = 690$ nm) nanosecond laser was used, the laser annealing led to intermixing of the silicon and germanium layers and to formation of their solid alloy [11]. Kolchin and coauthors [12] tried to crystallize amorphous Ge(10 nm)/Si(5 nm) MLs using a femtosecond laser ($\lambda = 1250$ nm, pulse duration 150 fs). However, regimes of selective Ge crystallization were not found, possibly due to too high laser fluences applied (above 100

* Corresponding author.
E-mail address: bulgakova@fzu.cz (N.M. Bulgakova).

https://doi.org/10.1016/j.optlastec.2023.109161
Received 22 July 2022; Received in revised form 2 December 2022; Accepted 9 January 2023

mJ/cm^2) for such ultrathin layers. Recently, we carried out successful experiments on selective crystallization of germanium layers in an amorphous Ge/Si ML stack using picosecond 1030-nm laser annealing [20]. In the present study, we have extended the irradiation conditions to longer wavelength (1500 nm) and shorter pulse duration (70 fs) and compared pico- and femtosecond PIRLA regimes with the aim to find optimal conditions for selective crystallization of Ge layers in Ge/Si ML stacks without crystallization of silicon and intermixing germanium and silicon layers.

2. Experimental

A multilayer a-Si:H/a-Ge:H stack consisting of 4 silicon (40-nm thick) and 3 germanium (15-nm thick) alternating amorphous layers was produced by plasma enhanced chemical vapor deposition (PECVD) on a Si(1 0 0) substrate with the top layer formed by a-Si. Monosilane (SiH_4) and monogermane (GeH_4) gases diluted by Ar were used as precursors for the Si and Ge layers, respectively. The temperature of the substrate during deposition was 225 °C. The thickness of the as deposited layers was controlled using a transmission electron microscope (TEM JEM-2200FS, 200 kV acceleration voltage) in the cross-section mode. For TEM measurements, a Si/Ge stack sample was first mechanically polished using a microscope Leica EM TXP and then thinned by a focused Ar ion beam. The presence of Si-H and Ge-H chemical bonds in the sample was analyzed using a Fourier transform infrared (FTIR) spectrometer FT-801 "Simex" with a spectral resolution of 4 cm^{-1}.

The multilayer Si/Ge stack was annealed by either a picosecond laser (HiLASE PERLA-B, $\lambda = 1030$ nm, pulse duration 1.4 ps, pulse energy up to 10 mJ) or a femtosecond laser (Astrella, Coherent) in combination with an optical parametric amplifier (TOPAS, Light Conversion) delivering a beam at $\lambda = 1500$ nm with a pulse duration of 70 fs and pulse energy up to 0.4 mJ. Both ps and fs pulses had Gaussian spatial and temporal profiles. The beams were focused at normal incidence on the sample surface by glass lenses onto circular spots of diameter $2\omega_0$ of 2.1 mm for 1030 nm and 0.53 mm for 1500 nm where ω_0 is the beam waist at the surface defined as the width at $1/e^2$ of the peak intensity. The ω_0 value was measured in every annealing experiment (see *Sec.* 3.2) by examining spot images using an Olympus BX43 optical microscope in Nomarski mode. The pulse energy E_0 was varied using a $\lambda/2$ plate in combination with a Glan polarizer to give a peak laser fluence $F_0 = 2E_0/\pi\omega_0^2$ in the range 20–200 mJ/cm^2. All the PIRLA experiments were performed under single shot irradiation conditions to avoid accumulation of defects in the stack under multi-shot irradiation [21,22] which apparently adversely affect the selective crystallization.

The phase composition of as-deposited and annealed ML stack was studied by Raman spectroscopy using a T64000 spectrometer with micro-Raman setup and a solid-state fiber laser (514.5 nm) as an excitation source. The excitation laser beam was focused to a 10-μm-diam spot at the center of the PIRLA-produced spots and thus the Raman spectra were collected from sites annealed uniformly at the peak laser fluence F_0.

3. Results and discussion

3.1. Characterization of the as deposited stack sample

Fig. 1 shows a cross-sectional TEM image of as-deposited a-Si:H/a-Ge:H ML stack. As is seen, the produced layers are identical in thickness, 15 nm for a-Ge and 40 nm for a-Si.

Fig. 2 shows a FTIR spectrum of the as-deposited a-Si:H/a-Ge:H ML stack in the range of valence mode vibrations of Ge-H and Si-H bonds. One can see two peaks with the strongest one at ~ 2000 cm^{-1} corresponding to Si-H bonds. Note that hydrogen from the SiH_4 precursor is mainly contained in Si-H bonds, not in Si-H_2 bonds, because the latter would result in a peak at ~ 2090 cm^{-1} [23]. The hydrogen atomic concentration in the Si layer can be estimated from these data as ~ 10 %

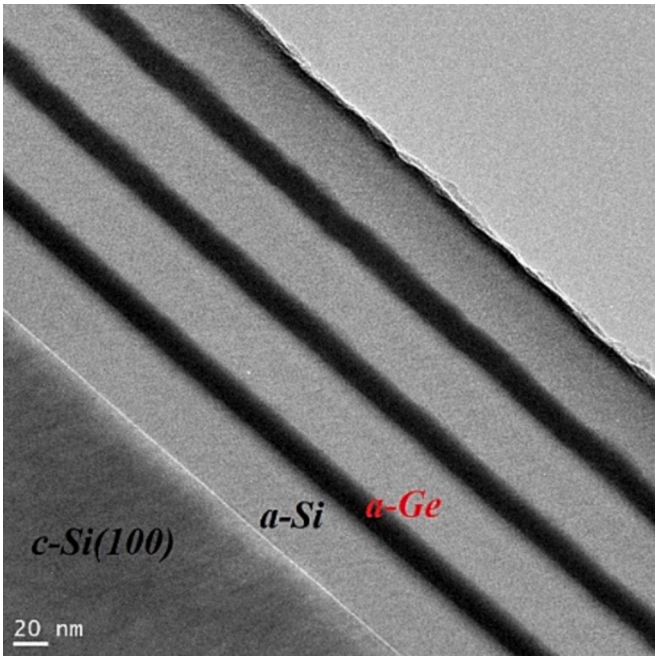

Fig. 1. TEM image of as-deposited a-Si:H/a-Ge:H ML stack. The dark fields are Ge layers.

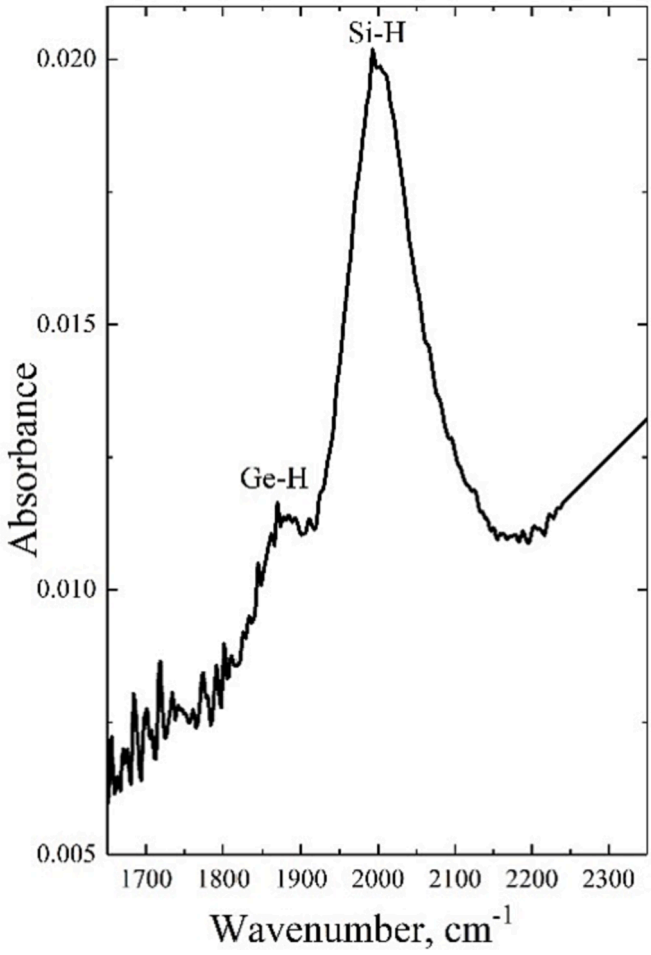

Fig. 2. FTIR spectrum of as-deposited a-Si:H/a-Ge:H MNLs.

using the IR-data-analysis method [24]. A weak peak at ~ 1880 cm^{-1} is related to valence mode vibrations Ge-H bonds [25]. This peak is considerably smaller than the Si-H peak, since, first, the thickness of the germanium layers is 2.7 times less than that of the silicon layers, second, the Ge-H bond is less strong and, third, the hydrogen concentration in the Ge layers is apparently lower than that in the Si layers as can be concluded based on correlations of the peak heights and the thickness of the layers. The last fact is favorable for the ultrashort PIRLA process since, at high hydrogen concentrations, dehydrogenation during rapid heating can cause damages in the layers.

3.2. Laser-induced damage and ablation of the Si/Ge ML stack

Fig. 3 shows optical images of typical spots produced at the ML stack surface by femtosecond 1500-nm laser pulses at different fluences. The general structure of the spot is similar to that observed for other materials, in particular for silicon crystals, irradiated by Gaussian laser pulses [10,26,27]. At sufficiently high laser fluences, three regions, corresponding to different local irradiation regimes within the spot, are clearly seen (Fig. 3,*c*). The central region 3 with a sharp boundary is the ablation zone. The middle region 2 also has a well-defined boundary and, according to [26], can be associated with the film damage and annealing, presumably due to melting of the top Si layer. The external, barely visible region 1 has a rather fuzzy outer boundary and is possibly due to silicon oxidation [26] and/or a modification of the upper Ge layer resulting in the change of contrast in the images. With further increase in laser fluence, several ablation regions are observed due to complete removal of top stack layers (Fig. 3,*d*). At fairly low fluences, below a threshold value for ablation, only the regions 1 and 2 are observed (Fig. 1,*a,b*).

An analysis of the spot optical images as a function of laser fluence allowed determining the effective irradiation spot size ω_0 and the threshold laser fluences for modification, damage and ablation of the investigated stack sample, $F_{th,m}$, $F_{th,d}$ and $F_{th,a}$. The analysis was based on the standard procedure for Gaussian beams when the damaged/ablated area S is related to the pulse energy E_0 by [28,29]

$$S = \frac{\pi\omega_0^2}{2}\ln(E_0/E_{th}) \quad (1)$$

where E_{th} is the corresponding threshold energy. By plotting the measured S values as a function of $\ln E_0$, we can obtain both the effective spot radius ω_0 and the threshold fluence $F_{th} = 2E_{th}/\pi\omega_0^2$. Fig. 4 shows such a plot for spots produced by 1500-nm, 70-fs pulses. The data yield good straight line fits in semilog plots confirming the Gaussian profile of the laser beam. The fits result in the spot diameter $2\omega_0 = 0.53$ mm and the modification, damage and ablation thresholds of 50, 70 and 115 mJ/cm^2, respectively. Similar spots were produced by irradiating the ML stack with 1030-nm, 1.4-ps laser pulses (although with considerably larger sizes) and very similar threshold values were obtained. All the measured modification, damage and ablation thresholds are summarized in Table 1. Note that, by properly adjusting the brightness and contrast of the Nomarski polarized light microscopy images, we were able to clearly identify the outer region boundary (Fig. 3,*a,b*) and thus to evaluate the corresponding modification thresholds.

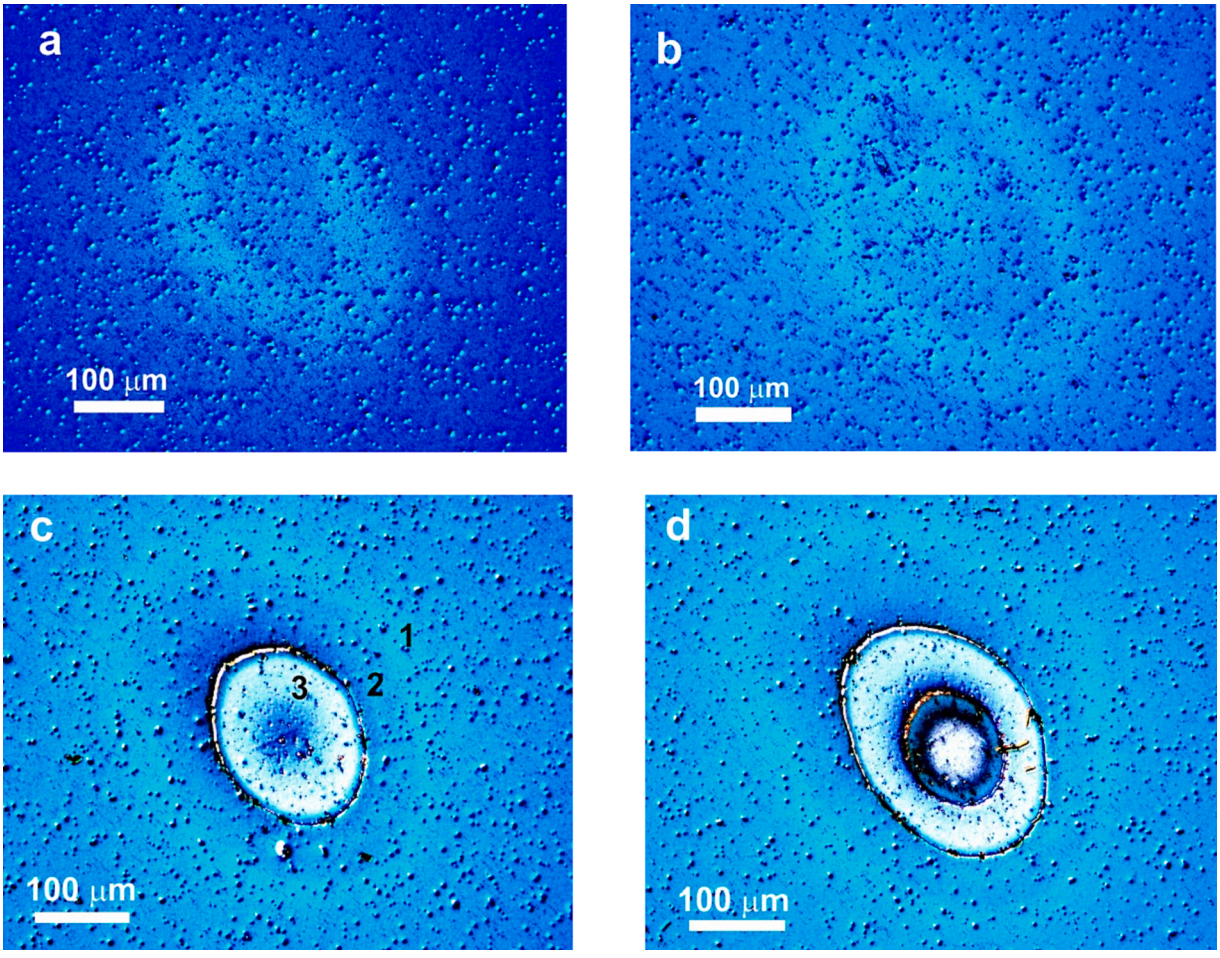

Fig. 3. Images of spots produced on the Si/Ge ML stack surface by single 1500-nm, 70-fs laser pulses at peak fluences of 77 (*a*), 95 (*b*), 145 (*c*) and 170 mJ/cm^2 (*d*). The numbers in (*c*) show modification (1), damage/annealing (2) and ablation (3) regions within the spot (see text for details).

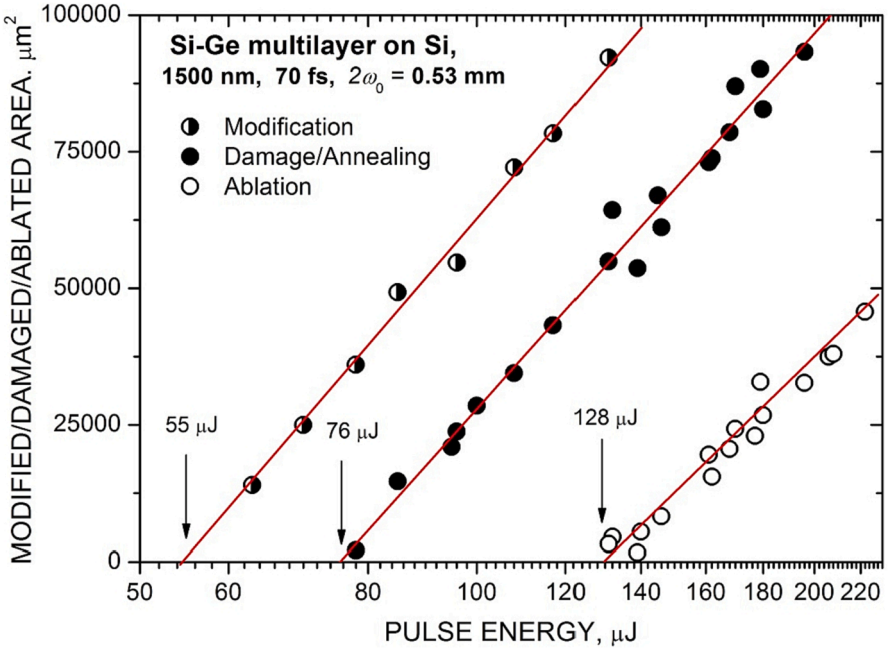

Fig. 4. Modified, damaged and ablated areas of spots produced on the Si/Ge ML stack surface by 1500-nm 70-fs laser pulses as a function of laser pulse energy. The lines represent the least-square fits according to Eq. (1). The measured threshold energies are indicated.

Table 1
Measured thresholds for Si/Ge ML stack modification ($F_{th,m}$), damage ($F_{th,d}$) and ablation ($F_{th,a}$) by ultrashort laser pulses.

Irradiation conditions	$F_{th,m}$	$F_{th,d}$	$F_{th,a}$, mJ/cm^2
1500 nm, 70 fs	50	70	115
1030 nm, 1.4 ps	45	65	110

3.3. Phase composition of the PIRLA-processed Si/Ge ML stack

Fig. 5 shows Raman spectra obtained after irradiation of the Si/Ge MLs at low laser fluences, below the damage threshold, for both fs and ps pulses. A Raman spectrum of the as-deposited ML stack is also shown. The latter contains broad bands at ~ 480 cm^{-1} and ~ 275 cm^{-1} related to the density of vibrational states of a-Si [23] and a-Ge [25], respectively. This indicates that all the layers are completely amorphous, since there are no peaks corresponding to mono- or nanocrystalline phases of silicon or germanium. It is known that the vibration frequencies of Ge–Si bonds are in the range from ~ 390 cm^{-1} to ~ 440 cm^{-1} [30]. In Ge/Si MLs, the Ge–Si bonds can be formed at hetero-boundaries, but, as one can see, the spectrum of the as-deposited MLs has no features at this frequency range. This indicates that the concentration of these mixed bonds is too low to be detected. Note that narrow peaks located at frequencies below 150 cm^{-1} are due to scattering on rotational-vibrational modes of the air molecules. It should be noted that the peak from the silicon substrate (520.6 cm^{-1}), which is usually very large, does not appear in the Raman spectra. There are two reasons for this. First, the polarization geometry Z(X'Y')-Z (in Porto notation) is forbidden for monocrystalline Si (1 0 0) orientation, where Z is (1 0 0), X' is (0 1 1) and Y' is (0 1 –1) crystallographic directions. The second reason is that green light is strongly absorbed by germanium. The penetration length in germanium is about 10 nm for photons with wavelength 514.5 nm. Therefore, 45 nm of germanium is sufficient to prevent the excitation source laser light from reaching the silicon substrate and scattering from it.

The PIRLA treatment of the Si/Ge stack at fairly low fluences, below 50 mJ/cm^2 for fs pulses and 40 mJ/cm^2 for ps pulses, i.e., below the measured modification thresholds, does not lead to changes in the

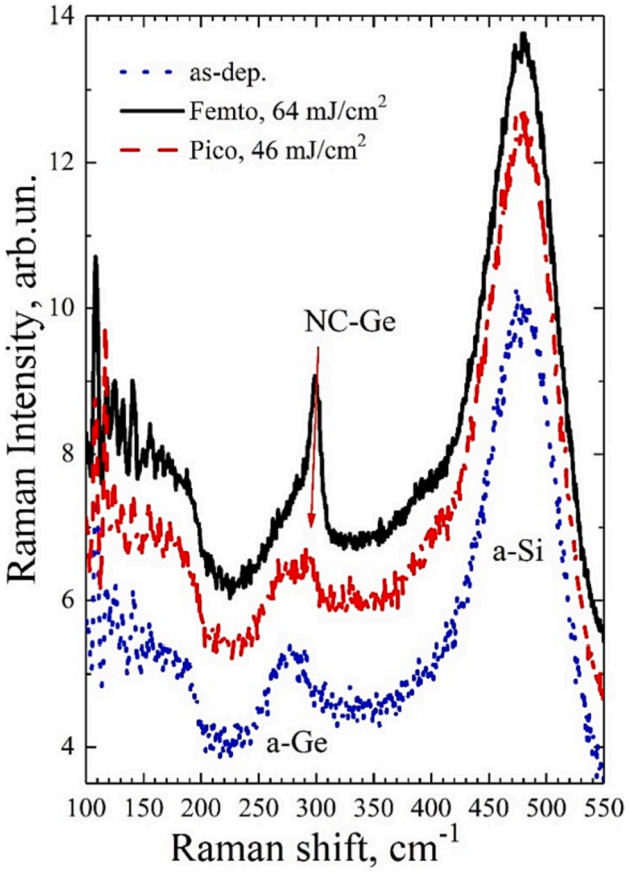

Fig. 5. Raman spectra of pulse-laser annealed Si/Ge ML stack, low fluences below the damage threshold. The arrow shows a small peak of Ge nanocrystals produced by ps PIRLA. The spectrum of the as-deposited sample is shown by the blue dotted line. (For interpretation of the references to colour in this figure legend, the reader is referred to the web version of this article.)

Raman spectra, and, therefore, does not cause noticeable structural transformations in the a-Ge/a-Si ML sample. After the ps PIRLA at a fluence of 46 mJ/cm^2, one can see a transformation of the broad a-Ge band – a narrower feature at a higher frequency of ~ 296 cm^{-1} appears against the background of the amorphous component (Fig. 5, dashed line). In monocrystalline Ge, the position of the peak for longwave optical phonons active in the Raman process is known to be 301.5 cm^{-1}. For nanocrystalline samples, according to the phonon confinement model (see [31] and references therein), the Raman peak is shifted towards lower frequencies and the smaller is the nanocrystal size, the larger is the shift. In the case of Ge nanocrystals (NCs), the observed shift of 5.5 cm^{-1} corresponds to the average NC size of about 3 nm [31]. Note that this size is much smaller than the thickness of the Ge layers (15 nm). In the case of femtosecond PIRLA at a fluence of 64 mJ/cm^2 (solid black curve, Fig. 3), the NC-Ge peak is higher and narrower, and its position is at about 298.5 cm^{-1} (Fig. 5 solid line) that corresponds to the average NC-Ge size of about 4.5 nm.

Fig. 6 shows Raman spectra obtained after irradiation of the Ge/Si ML stack at 70 mJ/cm^2, i.e., near the damage thresholds for both laser pulses (see Table 1). Again, the Raman spectra are quite similar for both fs and ps PIRLA. Under these irradiation conditions, the germanium layers are already almost completely crystallized, but there is slight intermixing with the silicon layers. This can be seen from the appearance of a Ge-Si peak at ~ 400 cm^{-1}. In the case of intermixing, it is no longer possible to accurately determine the size of Ge NCs, since these are no pure germanium nanocrystals, but nanocrystals from a Ge_xSi_{1-x} solid alloy. The position of the Raman peak depends now not only on the size of the NCs, but also on the stoichiometric parameter x [30]. In addition, the composition of the NCs can be inhomogeneous. Note, however, that in both cases the unmixed part of the silicon layers remains amorphous.

When laser fluence is increased above the ML stack damage threshold but still remains below the ablation threshold, laser-induced crystallization of the Si layers begins. This is manifested by the appearance of a narrow peak at ~ 510 cm^{-1} which is more pronounced at 1030-nm ps PIRLA (Fig. 7). According to the phonon confinement model for Si nanocrystals [32], their average size under these conditions is about 2 nm. With further increase in the fluence, above the ablation thresholds, almost complete intermixing of the germanium and silicon layers occurs (Fig. 8). Therewith, along with the main peak at 400 cm^{-1} related to the solid Si/Ge alloy, an additional peak appears at ~ 430 cm^{-1} (shown by the red arrow in Fig. 8) which is presumably due to local vibrations of Si atoms in Ge surroundings [30]. However, if the fluence is not too far from the ablation threshold, there is still a region of nanocrystalline silicon as manifested by the presence of a narrow peak at ~ 513 cm^{-1} (Fig. 8, fs pulses). The average size of the Si NCs is estimated to be about 3 nm in this case. At higher fluences the Si-NC peak disappears (Fig. 8, ps pulses) indicating that all the layers in the stack are intermixed. If we assume complete uniform intermixing, then, based on the Si and Ge layer thicknesses, the stoichiometric parameter x is expected to be about 0.3 and thus the Si-Si peak should be stronger than the Ge-Ge and Ge-Si peaks [30], which is not the case. One reason of this can be in the partial removal of silicon from the irradiation region due to ablation of the top Si layer. On the other hand, the Si-Si peak is wider than that observed for a homogeneous solid Ge_xSi_{1-x} alloy [30]. This indicates that, in our case, the GeSi solid alloy is rather inhomogeneous in composition and thickness variations of the x parameter are possible.

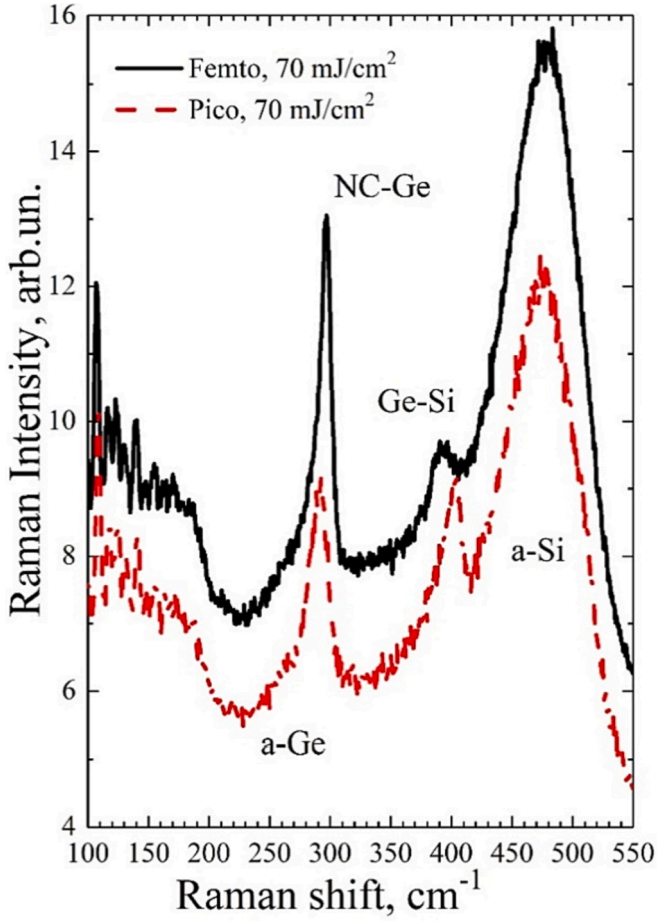

Fig. 6. Raman spectra of pulse-laser annealed Si/Ge ML stack, low-middle fluences near the damage threshold.

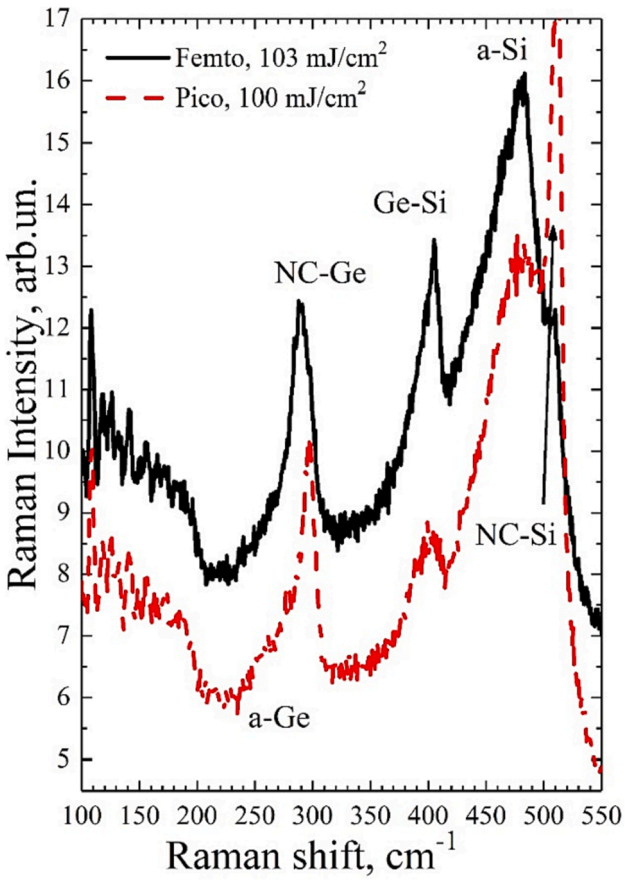

Fig. 7. Raman spectra of pulse-laser annealed Si/Ge ML stack, middle fluences above the damage threshold but below the ablation threshold. The arrow shows the peak of Si NCs produced by ps PIRLA.

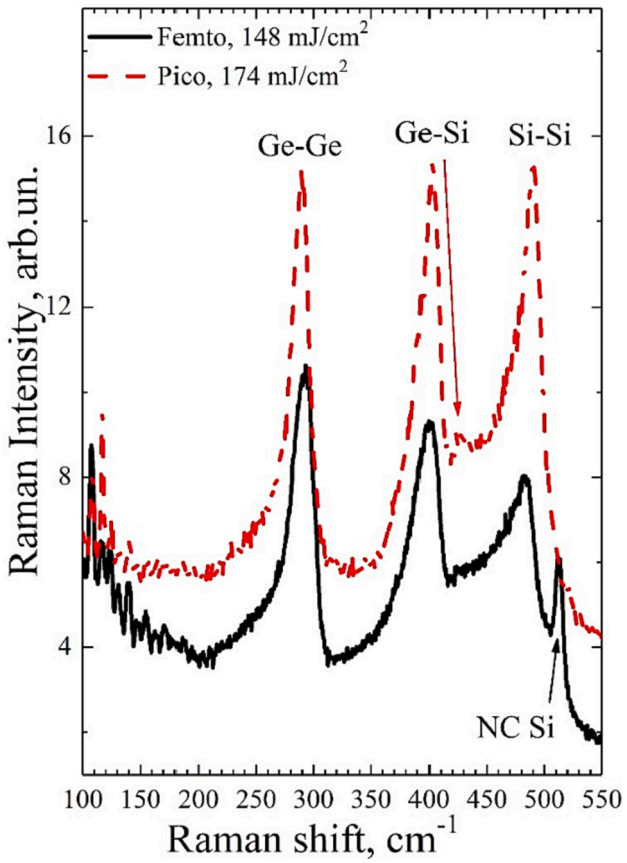

Fig. 8. Raman spectra of pulse-laser annealed Si/Ge ML stack, high fluences above the ablation threshold. The arrows show the peak of Si NCs produced by fs PIRLA and an additional peak of intermixed Si/Ge layers produced by ps PIRLA.

3.4. Analysis of ultrashort-laser-induced processes in Si and Ge layers in Ge/Si ML stacks

Irradiation of semiconductor materials by ultrashort laser pulses triggers a wealth of thermal and non-thermal processes in the irradiated samples [33–35]. When coupling with a bandgap material, a high-power laser beam generates free electrons via linear and/or non-linear photo-ionization (depending on the ratio between material band gap and photon energy). The electrons excited to the conduction band absorb laser energy and can become highly energetic, providing additional free electrons in the impact (avalanche) ionization. During femtosecond laser pulses, the lattice remains cold and, thus, the material occurs in a highly-nonequilibrium state whose relaxation to equilibrium takes place in picosecond time scale via electron–phonon coupling. For picosecond laser pulses, the electron-lattice relaxation proceeds already during laser action, thus providing some heating of the lattice before laser pulse termination. Ultrafast heating of a material results in stress generation, which can culminate in heated region destruction even in the solid state [36,37]. In semiconductors, ultrafast laser excitation of a dense free-electron plasma can lead to a phenomenon called ultrafast or cold melting [38–40]. In nanolayered structures considered here, the situation can be even more complicated, as the processes mentioned above can occur differently in adjacent layers, thus creating strong temperature gradients and a thermal expansion mismatch at interfaces. In this section, we analyze the major processes induced by ultrashort laser pulses in amorphous Ge and Si layers under the conditions of our experiments and consider their consequences for Ge/Si multilayer stacks. The optical and thermophysical properties of silicon and germanium used in the present estimations are given in Table 2.

Table 2
Optical and thermophysical properties of amorphous silicon and germanium used in the analysis.

Parameter	a-Si	a-Ge
Density, ρ, g/cm^3	2.28 [41]	5.15 [42]
Heat capacity, c_p, J/(kg K))	800 [41]	330 [43]
Melting temperature, T_m, K	1420 [41]	985 [44]
Heat of fusion, ΔH_m, J/kg	$1.25{\cdot}10^6$ [41]	$3.5{\cdot}10^5$ [44]
Band gap, E_g, eV	1.7 (direct) [45]	~0.45 [46]
One-photon absorption coefficient, α, 1/cm	0.4 at 1030 nm [47] 10^{-2} at 1500 nm [45]	$3{\cdot}10^4$ at 1030 nm [48] $2.35{\cdot}10^3$ at 1500 nm [48]
Two-photon absorption coefficient, β, cm/GW	2 at 1030 nm [49][a] 0.08 at 1550 nm [45]	taken as negligible for 1030 nm [b] 12 at 1500 nm [50]
Reflection coefficient, R	0.4 at 1030 nm [51] 0.31 at 1500 [51]	~0.43 at 1030 nm [48] ~0.4 at 1500 nm [48]
Young's modulus, E, GPa	134 [52]	126 [53]
Poisson ratio, ν	0.25 [52]	0.25 [54]
Linear thermal expansion coefficient, α_l, 1/K	$1{\cdot}10^{-6}$ [55]	$1.7{\cdot}10^{-5}$ (solid) [56] $0.9656{\cdot}10^{-4}$ (liquid) [57]
Rupture tensile strength, GPa	1.6 [58]	Unknown[c]

[a] Crystalline Si (no data available for a-Si at 1030 nm).
[b] Unknown for 1030 nm although calculations [50] show considerable reduction of 2PA with the photon energy thus implying the dominance of 1PA under considered conditions.
[c] Considered in estimations to be the same as for a-Si although expected to be somewhat smaller similar to crystalline Si and Ge [59].

Photo-ionization with generation of the free-electron plasma. In a general form, ionization kinetics in silicon under excitation by ultrashort near-infrared laser pulses can be described by the following rate equation [35,60]:

$$\frac{\partial n_e}{\partial t} = \frac{(1-R)\alpha I(z,t)}{\hbar\omega} + \frac{(1-R)^2\beta I^2(z,t)}{2\hbar\omega} + \delta(T_e)n_e - Cn_e^2 n_h \quad (2)$$

Here n_e and n_h is the free electron and hole densities respectively (usually assuming $n_e = n_h$); α and β are the one- and two-photon absorption (1PA and 2PA respectively) coefficients; I is the laser intensity; $\hbar\omega$ is the photon energy; $\delta(T_e)$ is the electron temperature dependent coefficient of collisional ionization; C is the Auger recombination coefficient. A similar framework can also be applied for germanium. For the sake of simplicity, we disregard in our analysis the impact ionization and recombination during the laser pulse in order to get a rough estimate of number of electrons excited by photoionization channels, which we consider here as the dominant processes. The expression for the estimations reads as

$$n_e \sim \frac{(1-R)\alpha I\tau}{\hbar\omega} + \frac{(1-R)^2\beta I^2\tau}{2\hbar\omega} = \frac{(1-R)\alpha F}{\hbar\omega} + \frac{(1-R)^2\beta F^2}{2\hbar\omega\tau} \quad (3)$$

where F is the incident laser fluence and τ is the laser pulse duration.

The results of the estimations of the free electron density for the conditions of irradiation by 1.4-ps, 1030-nm and 70-fs, 1500-nm laser pulses are presented in Tables 3 and 4 respectively. Contributions of the 1PA and 2PA processes are given in separate columns (except the case of a-Ge at 1030 nm where 1PA is dominant and 2PA may be disregarded). It is evident that, although for a-Si the two-photon absorption is the dominating process, the number density of the excited electrons is low, below 10^{20} cm^{-3}. Such excitation level cannot lead to a noticeable heating as will be shown below. On the contrary, for a-Ge, estimations show that the one-photon absorption is a governing process, which leads to generation of very high densities of free electrons although the 2PA process can also significantly contribute at 1500 nm laser wavelength. Having the data on the electron excitation and using energy balance considerations, one may estimate the resulting material heating.

Table 3
Results of estimations for 1.4-ps laser pulses at λ = 1030 nm of the electron number densities generated in 1PA and 2PA processes, lattice temperature expected after electron-lattice thermalization, and the fraction of the molten phase *f*.

Fluence, mJ/cm^2	a-Si			a-Ge			
	n_e, cm^{-3} (1PA)	n_e, cm^{-3} (2PA)	T, K	n_e, cm^{-3} (1PA)	$T_0 + \Delta T$, K	$T - f\Delta H_m$, K	f
40	$5.16{\cdot}10^{16}$	$2.14{\cdot}10^{18}$	300.7	$3.56{\cdot}10^{21}$	1121	985	0.128
55	$6.9{\cdot}10^{16}$	$4.05{\cdot}10^{18}$	301	$4.9{\cdot}10^{21}$	1430	985	0.42
70	$8.75{\cdot}10^{16}$	$6.56{\cdot}10^{18}$	302	$6.23{\cdot}10^{21}$	1737	985	0.709
100	$1.25{\cdot}10^{17}$	$1.34{\cdot}10^{19}$	304.2	$8.9{\cdot}10^{21}$	2353	1292	1
150	$1.88{\cdot}10^{17}$	$3{\cdot}10^{19}$	310	$1.34{\cdot}10^{22}$	3391	2330	1
190	$2.38{\cdot}10^{17}$	$4.83{\cdot}10^{19}$	316	$1.69{\cdot}10^{22}$	4198	3137	1

Table 4
The same as in Table 3 for 70-fs laser pulses at λ = 1500 nm.

Fluence, mJ/cm^2	a-Si			a-Ge				
	n_e, cm^{-3} (1PI)	n_e, cm^{-3} (2PI)	T, K	n_e, cm^{-3} (1PI)	n_e, cm^{-3} (2PI)	$T_0 + \Delta T$, K	$T - f\Delta H_m$, K	f
40	$2.16{\cdot}10^{15}$	$3.4{\cdot}10^{18}$	301	$7.86{\cdot}10^{20}$	$3.86{\cdot}10^{20}$	541	541	0
55	$2.96{\cdot}10^{15}$	$6.43{\cdot}10^{18}$	302	$1.34{\cdot}10^{21}$	$7.3{\cdot}10^{20}$	710	710	0
70	$3.77{\cdot}10^{15}$	$1.04{\cdot}10^{19}$	303.4	$1.95{\cdot}10^{21}$	$1.18{\cdot}10^{21}$	896	896	0
100	$5.39{\cdot}10^{15}$	$2.12{\cdot}10^{19}$	306.7	$3.5{\cdot}10^{21}$	$2.4{\cdot}10^{21}$	1370	985	0.36
150	$8.09{\cdot}10^{15}$	$4.78{\cdot}10^{19}$	315	$7.05{\cdot}10^{21}$	$5.4{\cdot}10^{21}$	2457	1396	1
190	$1.02{\cdot}10^{16}$	$7.64{\cdot}10^{19}$	325	$1.08{\cdot}10^{22}$	$8.7{\cdot}10^{21}$	3604	2543	1

Heating of a-Ge and a-Si layers; a-Ge melting and melt fraction. The thermalization between laser-excited hot electrons and lattice in semiconductors takes time of several picoseconds so that the thermal conduction can be disregarded on such timescales as a slow process. Hence, the local temperature increase $\Delta T = T - T_0$ (the initial temperature T_0 = 300 K) of the considered materials by ultrafast laser pulses can be roughly evaluated using the energy balance equation which can be written as

$$c_p \rho \Delta T = n_e \left(E_g + E^e_{\text{av}}\right) \quad (4)$$

Here c_p is the heat capacity, ρ is the density, E_g is the band gap, E^e_{av} is the average energy of free electrons generated by the laser pulse. We note that material heating at fluences above the melting threshold proceeds in three stages, namely (1) heating to the melting point, (2) the melting stage when material consumes the heat of fusion for lattice disordering, remaining at the melting temperature, (3) further heating of the melt to higher temperatures. Thus, the temperature rise obtained from Eq. (4) allows to estimate if the materials is heated to the melting point.

We note that, upon very rapid heating, solid materials can experience substantial superheating to a temperature $T^s_m > T_m$ at which a catastrophic homogeneous melting occurs [61–63]. The superheating level $(T^s_m - T_m)/T_m$ can reach values of 0.4 or even higher, depending on material properties and heating rate. Molecular dynamic studies [63] have revealed that, due to the nucleation catastrophe, the lattice temperature drops at the melting interface (boundary of complete melting) as a result of the energy expense for the latent heat of fusion (lattice destabilization). Hence, here we disregard the stage of transient overheating and evaluate the molten fraction as

$$f = c_p(T - T_m)/\Delta H_m \quad (5)$$

where ΔH_m is the heat of fusion. The condition $f \geq 1$ means complete melting and the temperature of the melt can be found from Eq. (4) by extraction of ΔH_m. We also note that the average energy of the excited free electrons can be considered at the level of ~ 2 eV at ultrashort laser heating to the temperature levels of melting point and slightly above [35], thus considering this value as E^e_{av} in our evaluations.

Using the described framework, we have evaluated the heating levels and the molten fractions for both germanium and silicon layers under our irradiation conditions, assuming for simplicity an insignificant attenuation of the laser beam in each nanolayer. The results are presented in Tables 3 and 4 for pico- and femtosecond pulses respectively. In all irradiation regimes studied, the estimations predict only minor heating of silicon nanolayers via their direct laser excitation. On the contrary, a-Ge nanolayers should be heated close to or above the melting point.

For ps irradiation regimes, germanium experiences partial melting at laser fluences from 40 mJ/cm^2 to 70 mJ/cm^2 (Table 3), which should result in the formation of nanocrystalline phase within amorphous matrix that agrees with the Raman spectra (Figs. 5 and 6). According to estimations, the fraction of molten phase increases from ~ 20 % at 46 mJ/cm^2 to 71 % at 70 mJ/cm^2. In this fluence range, no signs of a-Si crystallization have been detected while at 70 J/cm^2 a weak but distinct peak of Ge-Si intermixing starts to appear (Fig. 6). It can be explained by the enhanced mobility of Ge atoms in the molten zones, including Ge-Si interfaces, where covalent Ge-Si bonds can be formed. When laser fluence approaches and exceeds 100 mJ/cm^2 (Fig. 7), a-Ge nanolayers become molten completely (Table 3). They can partially transfer the heat to a-Si nanolayers for their heating that can be followed by formation of Si nanocrystals. Here we underline that, for ps irradiation regimes, the impact ionization process and free-electron plasma absorption can contribute to heating that is disregarded in the estimations for simplicity. Thus, the temperature levels in Table 3 may be somewhat underestimated. However, at $F \geq$ 150 mJ/cm^2, the evaluated temperature levels in a-Ge nanolayers indicate that heat transfer from molten germanium to a-Si nanolayers must lead to heating of a-Si above its melting point. As a result, molten Ge and Si nanolayers can efficiently mix that is indeed seen in Fig. 8.

The situation with fs laser pulses is more complicated. For laser fluences of 40–70 mJ/cm^2, the estimations show that a-Ge layers do not reach the melting point. Although impact ionization, if considered, may somewhat increase the evaluated temperature levels, we underline that this process is less efficient for fs pulses as compared to ps ones (impact ionization is insignificant for silicon at fs laser irradiation [35] that is even more applicable for Ge with the lower band gap). On the other hand, at fs laser pulses other processes such as stress formation and so-called ultrafast melting can influence the overall phenomenon of material crystallization. First, we evaluate the possibilities of strong stresses, which can lead to explosive crystallization of amorphous nanolayers [65–69].

Role of stresses; explosive crystallization. Upon annealing, amorphous semiconductor films experience thermal tensile stresses due to a

mismatch of the coefficient of thermal expansion with the substrate (between adjacent nanolayers in our case) [64]. As a result, nanocrystalline phase is formed even at moderate temperatures, well below the melting point. An external heat source, a laser or a particle beam, can induce stress in the locally heated amorphous film and trigger a process called explosive crystallization [65–69]. The heat released in explosive crystallization heats adjacent regions of amorphous material and thus provides a propagation of a "crystallization wave". When knowing the level of heating within the laser-irradiated spot, maximum stress can be evaluated as follows [70]:

$$\sigma_r^{max} = \frac{E\alpha_l \Delta T}{2(1-\nu)} \quad (6)$$

where E is Young's modulus, α_l is the coefficient of linear expansion, ΔT is the average temperature increase within the irradiation spot, and ν is the Poisson ratio. Using the data in Table 2, the stresses in a-Ge nanolayers upon irradiation at 1500 nm wavelength are evaluated to increase from 0.34 GPa at 40 mJ/cm^2 to 0.97 GPa at 100 mJ/cm^2. Thus, we may speculate that, in this fluence range, the efficient a-Ge solid phase crystallization without appearance of NC-Si and Ge-Si intermixing is possible due to strong stresses in relatively cold a-Ge nanolayers. We also note that the observed crystallization may be facilitated by the large mismatch between the coefficients of linear expansion of a-Ge and a-Si (see Table 2).

As shown recently via atomistic machine learning modeling [71], amorphous silicon under high pressure experiences a three-step transformation from the amorphous phase to nucleation of crystallites: (1) formation of coexisting polyamorphic low- and high-density regions; (2) structural collapse into a high-density amorphous phase; and (3) rapid nucleation of crystallites in this high-density phase. The authors of [71] subjected a-Si to a hydrostatic pressure at a constant rate of 100 MPa/ps with keeping the temperature well below the melting point (at 500 K). They found that applying such conditions was enough to overcome local energy barriers for structural transformation of the material towards a more stable crystalline form. In our case, the dynamic pressure at picosecond timescale can be even higher, up to several hundreds of MPa at sub-melting temperature levels. Furthermore, such transformation can be facilitated by the so-called 'non-thermal phase transition'.

Can the mechanism of ultrafast non-thermal phase transition promote a-Ge crystallization? Analyzing the data on the evaluated electron number density in Table 4, we note that, in fs irradiation regimes, the density of the ionized atoms in the a-Ge nanolayers approaches the criterium of ultrafast (non-thermal) phase transition [38–40]. It is accepted that, if a significant fraction (~10–15 %) of the valence electrons is pumped to the conduction band of semiconductors, the strong electronic excitation is almost immediately followed by bond softening and a sharp reduction of the average bonding-antibonding splitting, lattice destabilization, and the appearance of so called non-thermal melting already on a sub-ps time scale [72–76]. Although ultrafast destabilization of the lattice in already-disordered *amorphous* semiconductors looks to be rather difficult to observe, lattice atoms become mobile and can form crystallites as mentioned above. For low-bandgap semiconductors such as a-Ge, from the energy balance considerations one can expect a situation when "ultrafast melting" is not followed by thermal melting. Then, the destabilized lattice can build its more energetically stable crystalline form. However, this issue is beyond the scope of the present paper and calls for further investigations.

4. Conclusions

Pulsed infrared laser annealing (PIRLA) of thin amorphous layers of silicon and germanium in a multilayer Si/Ge stack has been performed using two IR lasers with picosecond (1030 nm) and femtosecond (1500 nm) pulse durations with the aim to find conditions for selective crystallization of the Ge layers. The phase composition of the irradiated sample was analyzed by Raman spectroscopy and the observed crystallization conditions were correlated with the measured laser-induced damage and ablation thresholds of the Si/Ge stack. Several regimes of PIRLA with increasing laser fluence are found for both picosecond and femtosecond laser pulses. (1) At low fluences, below the damage threshold, selective crystallization of germanium is observed when the Ge layers are crystallized into nanocrystals while the Si layers remain amorphous without noticeable intermixing of Ge and Si. (2) The Ge layers are almost fully crystallized without detectable Si crystallization but some Ge-Si intermixing occurs at fluences near the stack damage threshold. (3) Complete crystallization of the Ge layers with partial crystallization of Si layers and Ge-Si intermixing are observed at laser fluences above the damage threshold but below the ablation threshold. (4) Almost complete intermixing of the Ge and Si layers in the multilayer stack takes place at high laser fluences, above the ablation threshold. The crystallization and intermixing processes proceed similarly for the studied pico- and for the femtosecond PIRLA conditions.

A simple theoretical analysis involving evaluations of electron-hole generation, heating, molten fraction, and laser-induced stresses has been performed. It showed that in all experimental regimes, silicon layers can be heated only slightly by laser irradiation while germanium layers either approach or even overcome the melting point. It is concluded that intermixing of Ge and Si nanolayers at high laser fluences occurs due to heat transfer from molten Ge nanolayers to silicon, inducing melting of the latter. At optimal irradiation regimes when only germanium layers demonstrate crystallizations with no intermixing with silicon, stress-induced explosive crystallization may contribute to the phase transition process. The question on the possibility of ultrafast non-thermal phase transition is raised as the evaluated density of electron–phonon pairs is high and can induce destabilization of the amorphous lattice that however calls for further studies.

CRediT authorship contribution statement

V.A. Volodin: Conceptualization, Funding acquisition, Methodology, Investigation, Writing – original draft, Writing – review & editing. **Yuzhu Cheng:** Investigation. **A.V. Bulgakov:** Conceptualization, Methodology, Investigation, Writing – original draft, Writing – review & editing. **Y. Levy:** Investigation. **J. Beránek:** Investigation. **S.S. Nagisetty:** Investigation. **M. Zukerstein:** Investigation. **A.A. Popov:** Investigation, Resources. **N.M. Bulgakova:** Funding acquisition, Formal analysis, Validation, Visualization, Writing – original draft, Writing – review & editing.

Declaration of Competing Interest

The authors declare that they have no known competing financial interests or personal relationships that could have appeared to influence the work reported in this paper.

Data availability

No data was used for the research described in the article.

Acknowledgments

We are grateful to G.K. Krivyakin for the HRTEM measurements and to the Center for Collective Use "VTAN" NSU for providing equipment for Raman spectroscopy and HRTEM image analysis. The study of V.A.V. and Y.C. was supported by the Ministry of Science and Higher Education of the Russian Federation, project No. 075-15-2020-797 (13.1902.21.0024). A.V.B., Y.L., J.B., M.Z., and N.M.B. acknowledge support of the European Regional Development Fund and the state budget of the Czech Republic (project BIATRI: No. CZ.02.1.01/0.0/0.0/15_003/0000445). J.B. acknowledges also support of the Grant Agency of the Czech Technical University in Prague, grant No. SGS22/188/

OHK4/3T/14.

References

[1] T. Imajo, T. Ishiyama, N. Saitoh, N. Yoshizawa, T. Suemasu, K. Toko, Record-high hole mobility germanium on flexible plastic with controlled interfacial reaction, ACS Appl. Electron. Mater. 4 (2022) 269–275, https://doi.org/10.1021/acsaelm.1c00997.

[2] A.O. Zamchiy, E.A. Baranov, I.E. Merkulova, I.V. Korolkov, V.I. Vdovin, A. K. Gutakovskii, V.A. Volodin, Layer exchange during aluminum-induced crystallization of silicon suboxide thin films, Mater. Lett. 293 (2021), 129723, https://doi.org/10.1016/j.matlet.2021.129723.

[3] G. Fortunato, L. Mariucci, A. Pecora, V. Privitera, F. Simon, Chapter 1 - Historical evolution of pulsed laser annealing for semiconductor processing, in: F. Cristiano, A. La Magnal (Eds.), Laser Annealing Processes in Semiconductor Technology. Theory, Modeling and Applications in Nanoelectronics. Woodhead Publishing Series in Electronic and Optical Materials, Elsevier, 2021, pp. 1–48, https://doi.org/10.1016/C2019-0-01254-X.

[4] G.J. Lee, S.H. Song, Y.P. Lee, H. Cheong, C.S. Yoon, Y.D. Son, J. Jang, Arbitrary surface structuring of amorphous silicon films based on femtosecond-laser-induced crystallization, Appl. Phys. Lett. 89 (2006), 151907, https://doi.org/10.1063/1.2358922.

[5] V.A. Volodin, M.D. Efremov, G.A. Kachurin, A.G. Cherkov, M. Deutschmann, N. Baersch, Phase transitions in a-Si: H films on a glass irradiated by high-power femtosecond pulses: Manifestation of nonlinear and nonthermal effects, JETP Lett. 86 (2007) 119–122, https://doi.org/10.1134/S002136400714010X.

[6] O. Salihoglu, U. Kurum, H. Gul Yaglioglu, A. Elmali, A. Aydinli, Femtosecond laser crystallization of amorphous Ge, J. Appl. Phys. 109 (2011), 123108, https://doi.org/10.1063/1.3601356.

[7] O. Salihoglu, U. Kurum, H.G. Yaglioglu, A. Elmali, A. Aydinli, Crystallization of Ge in SiO_2 matrix by femtosecond laser processing, J. Vac. Sci. Technol. B 30 (2012), 011807, https://doi.org/10.1116/1.3677829.

[8] C. Korkut, K. Çınar, I. Kabaçelik, R. Turan, M. Kulakcı, A. Bek, Laser crystallization of amorphous Ge thin films via a nanosecond pulsed infrared laser, Cryst. Growth Des. 21 (2021) 4632, https://doi.org/10.1021/acs.cgd.1c00470.

[9] N. Farid, A. Brunton, P. Rumsby, S. Monaghan, R. Duffy, P. Hurley, M. Wang, K.-L. Choy, G.M. O'Connor, Femtosecond laser-induced crystallization of amorphous silicon thin films under a thin molybdenum layer, ACS Appl. Mater. Interfaces 13 (31) (2021) 37797, https://doi.org/10.1021/acsami.1c07083.

[10] C. Florian, D. Fischer, K. Freiberg, M. Duwe, M. Sahre, S. Schneider, A. Hertwig, J. Krüger, M. Rettenmayr, U. Beck, A. Undisz, J. Bonse, Single femtosecond laser-pulse-induced superficial amorphization and re-crystallization of silicon, Materials 14 (2021) 1651, https://doi.org/10.3390/ma14071651.

[11] V.A. Volodin, G.K. Krivyakin, G.D. Ivlev, S.L. Prokopyev, S.V. Gusakova, A. A. Popov, Crystallization of amorphous germanium films and multilayer a-Ge/a-Si structures upon exposure to nanosecond laser radiation, Semiconductors 53 (3) (2019) 400–405, https://doi.org/10.1134/S1063782619030217.

[12] A.V. Kolchin, D.V. Shuleiko, A.V. Pavlikov, S.V. Zabotnov, L.A. Golovan, D. E. Presnov, V.A. Volodin, G.K. Krivyakin, A.A. Popov, P.K. Kashkarov, Femtosecond laser annealing of multilayer thin film structures based on amorphous germanium and silicon, Tech. Phys. Lett. 46 (6) (2020) 560–563, https://doi.org/10.1134/S1063785020060048.

[13] K. Sugioka, Y. Cheng, Ultrafast lasers – reliable tools for advanced materials processing, Light Sci. Appl. 3 (2014) e149.

[14] R. Ricca, V. Boureau, Y. Bellouard, Ultrafast laser interaction with transparent multi-layer SiO_2/Si_3N_4 films, J. Appl. Phys. 130 (2021), 243105, https://doi.org/10.1063/5.0065726.

[15] S.V. Starinskiy, A.A. Rodionov, Y.G. Shukhov, A.I. Safonov, E.A. Maximovskiy, V. S. Sulyaeva, A.V. Bulgakov, Formation of periodic superhydrophilic microstructures by infrared nanosecond laser processing of single-crystal silicon, Appl. Surf. Sci. 512 (2020), 145753, https://doi.org/10.1016/j.apsusc.2020.145753.

[16] M. Zukerstein, J. Hrabovsky, J. Sladek, I. Mirza, Y. Levy, N.M. Bulgakova, Formation of tubular structures and microneedles on silicon surface by doughnut-shaped ultrashort laser pulses, Appl. Surf. Sci. 592 (2022), 153228, https://doi.org/10.1016/j.apsusc.2022.153228.

[17] T. Tiedje, J.M. Cebulka, Temperature dependence of the photoconductive absorption edge in amorphous silicon, Phys. Rev. B 28 (12) (1983) 7075, https://doi.org/10.1103/PhysRevB.28.7075.

[18] R.V. Kruzelecky, C. Ukah, D. Racansky, S. Zukotynski, J.M. Perz, Intraband optical absorption in amorphous silicon, J. Non-Cryst. Solids 103 (1988) 234, https://doi.org/10.1016/0022-3093(88)90202-5.

[19] Z. Remes, J. Stuchlik, J. The-ha Stuchlikova, V. Kupcik, A. Mortet, P. Taylor, V.A. V. Ashcheulov, Electroluminescence of thin film *p-i-n* diodes based on a-SiC: H with integrated Ge nanoparticles, Eur. Phys. J. Appl. Phys. 88 (2019) 30302, https://doi.org/10.1051/epjap/2020190253.

[20] V.A. Volodin, G.K. Krivyakin, A.V. Bulgakov, Y. Levy, J. Beránek, S. Nagisetty, Z. Bryknar, N.M. Bulgakova, P.V. Geydt, A.A. Popov, Picosecond infrared laser crystallization of Ge layers in Ge/Si multi-nanolayers for optoelectronic applications, Proc. SPIE 12157 (2022) 1215702, https://doi.org/10.1117/12.2622731.

[21] E. Coyne, J.P. Magee, P. Mannion, G.M. O'Connor, T.G. Glynn, Characterisation of laser ablation of silicon using a Gaussian wavefront and computer generated wavefront reconstruction, Appl. Surf. Sci. 229 (2004) 148–160, https://doi.org/10.1016/j.apsusc.2004.01.068.

[22] O. Armbruster, A. Naghilou, M. Kitzler, W. Kautek, Spot size and pulse number dependence of femtosecond laser ablation thresholds of silicon and stainless steel, Appl. Surf. Sci. 396 (2017) 1736–1740, https://doi.org/10.1016/j.apsusc.2016.11.229.

[23] M.H. Brodsky, Manuel Cardona, J.J. Cuomo, Infrared and Raman spectra of the silicon-hydrogen bonds in amorphous silicon prepared by glow discharge and sputtering, Phys. Rev. B 16 (1977) 3556–3571, https://doi.org/10.1103/PhysRevB.16.3556.

[24] A.A. Langford, M.L. Fleet, B.P. Nelson, W.A. Lanford, N. Maley, Infrared absorption strength and hydrogen content of hydrogenated amorphous silicon, Phys. Rev. B 45 (1992) 13367–13377, https://doi.org/10.1103/PhysRevB.45.13367.

[25] B.K. Ghosh, B.K. Agrawal, Vibrational excitations in a-Ge:F, H alloys, Phys. Rev. B 33 (1986) 1250–1256, https://doi.org/10.1103/PhysRevB.33.1250.

[26] J. Bonse, S. Baudach, J. Krüger, W. Kautek, M. Lenzner, Femtosecond laser ablation of silicon-modification thresholds and morphology, Appl. Phys. A 74 (2002) 19–25, https://doi.org/10.1007/s003390100893.

[27] K. Werner, V. Gruzdev, N. Talisa, K. Kafka, D. Austin, C.M. Liebig, E. Chowdhury, Single-shot multi-stage damage and ablation of silicon by femtosecond mid-infrared laser pulses, Sci. Rep. 9 (2019) 19993, https://doi.org/10.1038/s41598-019-56384-0.

[28] J.M. Liu, Simple technique for measurements of pulsed Gaussian-beam spot sizes, Opt. Lett. 7 (1982) 196–198, https://doi.org/10.1364/OL.7.000196.

[29] S.V. Starinskiy, Y.G. Shukhov, A.V. Bulgakov, Laser-induced damage thresholds of gold, silver and their alloys in air and water, Appl. Surf. Sci. 396 (2017) 1765–1774, https://doi.org/10.1016/j.apsusc.2016.11.221.

[30] V.A. Volodin, M.D. Efremov, A.S. Deryabin, L.V. Sokolov, Determination of the composition and stresses in $Ge_xSi_{(1-x)}$ heterostructures from Raman spectroscopy data: Refinement of model parameters, Semiconductors 40 (2006) 1314–1320, https://doi.org/10.1134/S106378260611011X.

[31] V.A. Volodin, D.V. Marin, V.A. Sachkov, E.B. Gorokhov, H. Rinnert, M. Vergnat, Applying of improved phonon confinement model for analysis of Raman spectra of germanium nanocrystals, J. Exp. Theor. Phys. 118 (2014) 65–71, https://doi.org/10.1134/S1063776114010208.

[32] V.A. Volodin, V.A. Sachkov, Improved model of optical phonon confinement in silicon nanocrystals, J. Exp. Theor. Phys. 116 (2013) 87–94, https://doi.org/10.1134/S1063776112130183.

[33] J.K. Chen, D.Y. Tzou, J.E. Beraun, Numerical investigation of ultrashort laser damage in semiconductors, Int. J. Heat Mass Transf. 48 (2005) 501–509, https://doi.org/10.1016/j.ijheatmasstransfer.2004.09.015 72.

[34] N.M. Bulgakova, I.M. Burakov, Y.P. Meshcheryakov, R. Stoian, A. Rosenfeld, I. V. Hertel, Theoretical models and qualitative interpretations of fs material processing, J. Laser Micro Nanoeng. 2 (2007) 76–86, https://doi.org/10.2961/jlmn.2007.01.0014.

[35] A. Rämer, O. Osmani, B. Rethfeld, Laser damage in silicon: Energy absorption, relaxation, and transport, J. Appl. Phys. 116 (2014), 053508, https://doi.org/10.1063/1.4891633.

[36] K. Sokolowski-Tinten, W. Ziegler, D. von der Linde, M.P. Siegal, D.L. Overmyer, Short-pulse-laser-induced optical damage and fracto-emission of amorphous, diamond-like carbon films, Appl. Phys. Lett. 86 (2005), 121911, https://doi.org/10.1063/1.1888037.

[37] S. Rapp, J. Rosenberger, M. Domke, G. Heise, H.P. Huber, M. Schmidt, Ultrafast pump-probe microscopy reveals the mechanism of selective fs laser structuring of transparent thin films for maskless micropatterning, Appl. Surf. Sci. 290 (2014) 368–372, https://doi.org/10.1016/j.apsusc.2013.11.086.

[38] C.V. Shank, R. Yen, C. Hirlimann, Time-resolved reflectivity measurements of femtosecond-optical-pulse-induced phase transitions in silicon, Phys. Rev. Lett. 50 (1983) 454–457, https://doi.org/10.1103/PhysRevLett.50.454.

[39] K. Sokolowski-Tinten, C. Blome, C. Dietrich, A. Tarasevitch, M. Horn von Hoegen, D. von der Linde, A. Cavalleri, J. Squier, M. Kammler, Femtosecond X-ray measurement of ultrafast melting and large acoustic transients, Phys. Rev. Lett. 87 (2001), 225701, https://doi.org/10.1103/PhysRevLett.87.225701.

[40] A. Rousse, C. Rischel, S. Fourmaux, I. Uschmann, S. Sebban, G. Grillon, P.h. Balcou, E. Förster, J.P. Geindre, P. Audebert, J.C. Gauthier, D. Hulin, Non-thermal melting in semiconductors measured at femtosecond resolution, Nature 410 (2001) 65–68, https://doi.org/10.1038/35065045.

[41] D. Bäuerle, Laser Processing and Chemistry, fourth ed., Springer-Verlag, Berlin Heidelberg, 2011.

[42] D. Goldschmidt, Amorphous germanium as a medium temperature solar selective absorber, Thin Solid Films 90 (1982) 139–143, https://doi.org/10.1016/0040-6090(82)90633-2.

[43] H.S. Chen, D. Turnbull, Specific heat and heat of crystallization of amorphous germanium, J. Appl. Phys. 40 (1969) 4214–4215, https://doi.org/10.1063/1.1657175.

[44] W. Szyszko, F. Vega, C.N. Afonso, Shifting of the thermal properties of amorphous germanium films upon relaxation and crystallization, Appl. Phys. A 61 (1995) 141–147, https://doi.org/10.1007/BF01538380.

[45] Y. Shoji, T. Ogasawara, T. Kamei, Y. Sakakibara, S. Suda, K. Kintaka, H. Kawashima, M. Okano, T. Hasama, H. Ishikawa, M. Mori, Ultrafast nonlinear effects in hydrogenated amorphous silicon wire waveguide, Opt. Express 18 (2010) 5668–5673, https://doi.org/10.1364/OE.18.005668.

[46] E.S.M. Goh, T.P. Chen, C.Q. Sun, Y.C. Liu, Thickness effect on the band gap and optical properties of germanium thin films, J. Appl. Phys. 107 (2010), 024305, https://doi.org/10.1063/1.3291103.

[47] C. Boyuan, Amorphous silicon thin film solar cells with engineered nanoparticles, LAP Lambert Academic Publishing, 2015.

[48] H. Liu, S. Li, P. Sun, X. Yang, D. Liu, Y. Ji, F. Zhang, D. Chen, Y. Cui, Study on characterization method of optical constants of germanium thin films from absorption to transparent region, Mater. Sci. Semicond. Process. 83 (2018) 58–62, https://doi.org/10.1016/j.mssp.2018.04.019.
[49] A.D. Bristow, N. Rotenberg, H.M. van Driel, Two-photon absorption and Kerr coefficients of silicon for 850–2200 nm, Appl. Phys. Lett. 90 (2007), 191104, https://doi.org/10.1063/1.2737359.
[50] H. Garcia, K.N. Avanaki, Direct and indirect two-photon absorption in Ge within the effective mass approximation, Appl. Phys. Lett. 100 (2012), 131105, https://doi.org/10.1063/1.3693389.
[51] E.D. Palik, Handbook of Optical Constants of Solids, Academic Press, 1985.
[52] R. Kuschnereit, H. Fath, A.A. Kolomenskii, M. Szabadi, P. Hess, Mechanical and elastic properties of amorphous hydrogenated silicon films studied by broadband surface acoustic wave spectroscopy, Appl. Phys. A 61 (1995) 269–276, https://doi.org/10.1007/BF01538192.
[53] T. Zhan, Y. Xu, M. Goto, Y. Tanaka, R. Kato, M. Sasaki, Y. Kagawa, Thermal conductivity of sputtered amorphous Ge films, AIP Adv. 4 (2014), 027126, https://doi.org/10.1063/1.4867122.
[54] J. Bharathan, J. Narayan, G. Rozgonyi, E. Bulman, Poisson Ratio of Epitaxial Germanium Films Grown on Silicon, J. Electron. Mater. 42 (2013) 40–46, https://doi.org/10.1007/s11664-012-2337-6.
[55] K. Takimoto, A. Fukuta, Y. Yamamoto, N. Yoshida, T. Itoh, S. Nonomura, Linear thermal expansion coefficients of amorphous and microcrystalline silicon films, J. Non-Cryst. Solids 299–302 (2002) 314–317, https://doi.org/10.1016/S0022-3093(02)00930-4.
[56] P.D. Persans, A.F. Ruppert, Thermal expansion of hydrogenated amorphous germanium thin films, J. Appl. Phys. 59 (1986) 271–273, https://doi.org/10.1063/1.336824.
[57] W.-K. Rhim, T. Ishikawa, Thermophysical properties of molten germanium measured by a high-temperature electrostatic levitator, Int. J. Thermophys. 21 (2000) 429–443, https://doi.org/10.1023/A:1006639714415.
[58] K.L. Brookshire, Mechanical characterization of amorphous Si-based thin films for large area MEMS, PhD thesis, University of Western Australia, 2016.
[59] A.L. Ruoff, On the ultimate yield strength of solids, J. Appl. Phys. 49 (1978) 197–200, https://doi.org/10.1063/1.324321.
[60] H.M. van Driel, Kinetics of high-density plasmas generated in Si by 1.06- and 0.53-μm picosecond laser pulses, Phys. Rev. B 35 (1987) 8166–8176, https://doi.org/10.1103/PhysRevB.35.8166.
[61] K. Lu, Y. Li, Homogeneous nucleation catastrophe as a kinetic stability limit for superheated crystal, Phys. Rev. Lett. 80 (1998) 4474–4477, https://doi.org/10.1103/PhysRevLett.80.4474.
[62] B. Rethfeld, V.V. Temnov, K. Sokolowski-Tinten, P. Tsu, D. von der Linde, S. I. Anisimov, S.I. Ashitkov, M.B. Agranat, Superfast thermal melting of solids under the action of femtosecond laser pulses, J. Opt. Technol. 71 (2004) 348–352, https://doi.org/10.1364/JOT.71.000348.
[63] D.S. Ivanov, L.V. Zhigilei, Kinetic limit of heterogeneous melting in metals, Phys. Rev. Lett. 98 (2007), 195701, https://doi.org/10.1103/PhysRevLett.98.195701.
[64] J. Park, S. Kwon, S.-I. Jun, I.N. Ivanov, J. Cao, J.L. Musfeldt, P.D. Rack, Stress induced crystallization of hydrogenated amorphous silicon, Thin Solid Films 517 (2009) 3222–3226, https://doi.org/10.1016/j.tsf.2008.10.114.
[65] R.K. Sharma, S.K. Bansal, R. Nath, R.M. Mehra, K. Bahadur, R.P. Mall, K. L. Chaudhary, C.L. Garg, Electron beam induced explosive crystallization of unsupported amorphous germanium thin films, J. Appl. Phys. 55 (1984) 384–387, https://doi.org/10.1063/1.333085.
[66] C. Césari, G. Nihoul, J. Marfaing, W. Marine, B. Mutaftschiev, Amorphous-crystalline interfaces after laser induced explosive crystallization in amorphous germanium, Surf. Sci. 162 (1985) 724–730, https://doi.org/10.1016/0039-6028(85)90972-0.
[67] V.A. Volodin, A.S. Kachko, A.G. Cherkov, A.V. Latyshev, J. Koch, B.N. Chichkov, Femtosecond Pulse Crystallization of Thin Amorphous Hydrogenated Films on Glass Substrates Using Near Ultraviolet Laser Radiation, JETP Lett. 93 (2011) 603–606, https://doi.org/10.1134/S0021364011100134.
[68] V.A. Volodin, A.S. Kachko, Crystallization of hydrogenated amorphous silicon films by exposure to femtosecond pulsed laser radiation, Semiconductors 45 (2011) 265–270, https://doi.org/10.1134/S1063782611020254.
[69] L. Nikolova, M.J. Stern, J.M. MacLeod, B.W. Reed, H. Ibrahim, G.H. Campbell, F. Rosei, T. LaGrange, B.J. Siwick, *In situ* investigation of explosive crystallization in a-Ge: Experimental determination of the interface response function using dynamic transmission electron microscopy, J. Appl. Phys. 116 (2014), 093512, https://doi.org/10.1063/1.4894397.
[70] Y.P. Meshcheryakov, N.M. Bulgakova, Thermoelastic modeling of microbump and nanojet formation on nanosize gold films under femtosecond laser irradiation, Appl. Phys. A 82 (2006) 363–368, https://doi.org/10.1007/s00339-005-3319-9.
[71] V.L. Deringer, N. Bernstein, G. Csányi, C. Ben Mahmoud, M. Ceriotti, M. Wilson, D. A. Drabold, S.R. Elliott, Origins of structural and electronic transitions in disordered silicon, Nature 589 (2021) 59–64, https://doi.org/10.1038/s41586-020-03072-z.
[72] J.A. Van Vechten, R. Tsu, F.W. Saris, Nonthermal pulsed laser annealing of Si; plasma annealing, Phys. Let. A 74 (1979) 422–426, https://doi.org/10.1016/0375-9601(79)90242-1.
[73] P. Stampfli, K.H. Bennemann, Theory for the instability of the diamond structure of Si, Ge, and C induced by a dense electron-hole plasma, Phys. Rev. B 42 (1990) 7163–7173, https://doi.org/10.1103/PhysRevB.42.7163.
[74] K. Sokolowski-Tinten, J. Bialkowski, D. von der Linde, Ultrafast laser-induced order-disorder transitions in semiconductors, Phys. Rev. B 51 (1995) 14186–14198, https://doi.org/10.1103/PhysRevB.51.14186.
[75] S.K. Sundaram, E. Mazur, Inducing and probing non-thermal transitions in semiconductors using femtosecond laser pulses, Nat. Mat. 1 (2002) 217–224, https://doi.org/10.1038/nmat767.
[76] V. Tkachenko, M.M. Abdullah, Z. Jurek, N. Medvedev, V. Lipp, M. Makita, B. Ziaja, Limitations of Structural Insight into Ultrafast Melting of Solid Materials with X-ray Diffraction Imaging, Appl. Sci. 11 (2021) 51572, https://doi.org/10.3390/app11115157.